Article

Delayed fracture behavior of ultra-high-strength mooring chain steel evaluated by potentiostatic hydrogen-charging combined with SSRT

Check for updates

Jiajiao Wei[1], Ke Hou[1], Feng Yang[1], Zhipeng Chang[1], Ju Li[1], Yunliang Shao[2], Mengjia Li[3], Xiaomei Yu[1], Jinyou Zheng[1], Yutao Zhou[4], Yongpeng Yang[5], Dehai Ping[6], Yong Liu[1], Min Li[1] & Songjie Li [1]✉

The influence of hydrogen charging potentials on the hydrogen embrittlement susceptibility of R6 ultra-high strength mooring chain steel was investigated via constant potential hydrogen charging slow strain rate tensile tests combined with thermal desorption analysis. The results reveal that hydrogen charging leads to a 38.94% decrease in elongation, while the impact on tensile strength is relatively minor. Furthermore, the specimens experienced intergranular cracking at the critical potential of −1150 mV, with the size of the brittle region increasing as the negative charging potential becomes more negative. And, hydrogen atoms can cause local embrittlement of materials and increase KAM value.

The mooring chain is a key component for the positioning of offshore units such as drilling rigs, production systems, buoys, and floating wind turbines. The chains are made of alloyed steel and classified as R3, R3S, R4, R4S, R5, and R6 based on the tensile strength. For example, R6 has the highest tensile strength of approximately 1100 MPa[1]. As the strength increases, the chain steel becomes more susceptible to hydrogen[2–4], while served in seawater. In consequence, the high-grade mooring chains are applied in a more prudent manner, mostly on mobile offshore units (MOU) which are temporarily deployed for exploration and migrated from time to time. Moreover, the high-grade chains are also used with limited hardness, i.e. HB330 for R4S and HB340 for R5 as specified in ABS rule[5].

Even though failures of R5 chains have been reported by DNV-DET NORSKE VERITAS (DNV)[6,7] recently. Two kinds of fractures were defined in these studies: (1) cracks in the straight area relating to untempered martensite generated by improper handling during installation; and (2) cracks at the inner bend where plastic deformation was found accompanying with inter-link wear. In both cases, the surface hardness was found higher than the normal situation. Significant corrosion was also observed on the link surfaces. Meanwhile, some fracture surfaces showed intergranular fracture, while secondary cracking was found by metallographic inspection of the cross-section. The current study attributes the failure mechanism to abnormal microstructure resulting from anchor chain handling operations, but also takes into account the high load and cathodic protection (CP) of vessels.

As presented by DNV, corrosion and CP are the main sources of hydrogen. The corrosion behavior of mooring chain steels with different environmental conditions has been studied in past years[8–11]. Furthermore, the influence of corrosion on chain mechanical properties in conjunction with various loads was also investigated[12–16]. Although, only a few researches were performed with simulated CP conditions on the effect of potential, salinity, temperature, and dissolved oxygen[17,18], most studies were focused on the materials. However, the environmental hydrogen content and its relationship with applied potential have not been qualitatively revealed so far. In addition, more works are required to investigate the side effects of CP on high-strength mooring chains to guide further applications. CP has been widely used in the offshore industry to protect floating units as an effective anti-corrosion method for hull structures. Generally, the chains are not intentionally covered by the CP system, but in many cases, at least 30 m chains should be taken into consideration during the design of CP. To maintain the protection effect in a service life of more than 20 years, the CP

[1]School of Chemical Engineering, Zhengzhou University, 100 Science Avenue, Zhengzhou 450001, P. R. China. [2]Key lab of mooring chain design and application technology, Asian Star Anchor Chain Co., Ltd., Jingjiang, Jiangsu 214500, P. R. China. [3]School of Materials Science and Engineering, Zhengzhou University, 100 Science Avenue, Zhengzhou 450001, P. R. China. [4]College of Material and Advanced Manufacturing, Hunan University of Technology, Zhuzhou, Hunan 412007, China. [5]Henan Institute of Advanced Technology, Zhengzhou University, Zhengzhou 450003, China. [6]Zhongyuan Critical Metals Laboratory, Zhengzhou University, 100 Science Avenue, Zhengzhou 450001, P. R. China. ✉e-mail: songjie@zzu.edu.cn

systems must be designed with an overcapacity to meet the requirements[19]. As recommended by ABS[20] and DNV[21], a protection potential of −800 mV or more negatively measured concerning the Ag/AgCl seawater reference electrode is acceptable. The detrimental effects of CP on steel are also identified thus a hardness limitation of HV350 is suggested to lower the risk of hydrogen-induced stress cracking (HISC). However, the chains of R6 and lower grades of steels subjected to improper heat treatment generally have a hardness higher than the upper limit. As a result, these cases put the chains in a dangerous situation where more hydrogen is introduced especially for the high-strength mooring chains. Therefore, the lack of knowledge on HISC behavior of high-strength mooring chains calls for more studies in this field. This paper will focus on the effect of charging potential on the mechanical properties and delayed fracture behavior of R6 chains via slow strain rate tensile testing and thermal desorption analysis.

Results and discussion
Microstructure
X-ray diffraction (XRD) was utilized to analysis the R6-grade mooring chain steel, the result is depicted in Fig. 1. Distinct diffraction peaks are observed
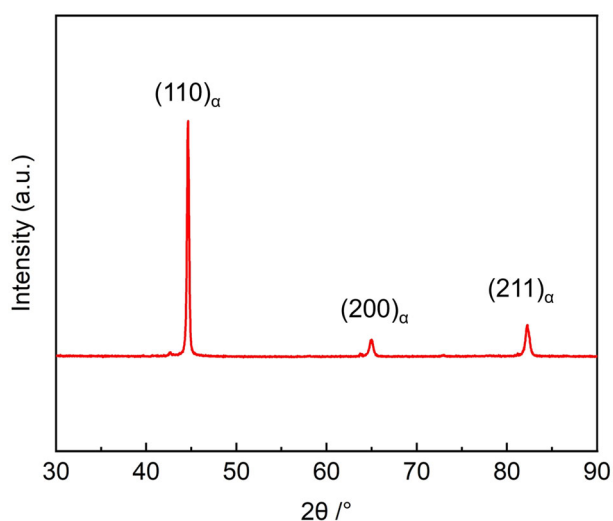

Fig. 1 | X-ray diffraction (XRD) crystal structure analysis of R6 mooring chain steel.

near 45°, 65°, and 82°, all of which correspond to the diffraction peaks of α-Fe[22,23]. This indicates that the R6-grade mooring chain steel is composed of a single body-centered cubic (BCC) phase, with no presence of residual austenite or other microstructural features.

Figure 2 shows the initial microstructure of the mooring chain steel. The phase map (Fig. 2a) reveals a series of parallel strip-like structures, indicating that the microstructure is predominantly composed of lath martensite. It can be observed that the microstructure exhibits a uniform BCC structure. The inverse pole figure (IPF) map of the sample (Fig. 2b) illustrates different colored grains representing distinct crystallographic orientations, with similar colors indicating similar grain orientations. Figure 2c, f presents the recrystallization distribution map of the sample along with its statistical results. In the figure, the blue color represents recrystallized grains, the yellow color represents substructures, and the red color represents deformed grains. It can be observed from the figure that the percentage of recrystallized grains is relatively low, accounting for only 4.8% of the total. The predominant grain population consists of substructured grains, accounting for 74.1%, while deformed grains constitute 21.1%.

The misorientation angle grain boundary map is shown in Fig. 2d. The misorientation angle (θ) exceeds 15°, which is classified as high-angle grain boundaries (HAGBs) indicated by green lines, whereas the misorientation angle (θ) is within the range of 2° to 15°, which is classified as low-angle grain boundaries (LAGBs) depicted by red lines[24]. It can be observed that the volume fractions of HAGBs and LAGBs in the original sample are 68% and 32%, respectively. The Kernel Average Misorientation (KAM) map quantifies the average orientation difference between a given point and its neighboring points within the same grain[25]. Figure 2e illustrates that the initial microstructure possesses a mean KAM value of 0.66, which denotes a comparatively modest dislocation density[26].

Electrochemical experiment analysis
Cathodic polarization curve testing was conducted to determine the hydrogen evolution potential of the specimen, which obtained the range of cathodic polarization potential for subsequent experiments. The polarization curve of the investigated specimen was plotted, as shown in Fig. 3. The passivation effect gives rise to a current plateau in the anodic polarization curve, ranging from −696 mV to −576 mV (Ag/AgCl), where the current density remains relatively constant. Subsequently, the passivation coating ruptures at −576 mV (Ag/AgCl), resulting in a sudden increase in the current density. The transition of the cathodic reaction of R6 mooring chain steel from oxygen concentration diffusion control to hydrogen evolution activation control occurs when the hydrogen charging potential reaches
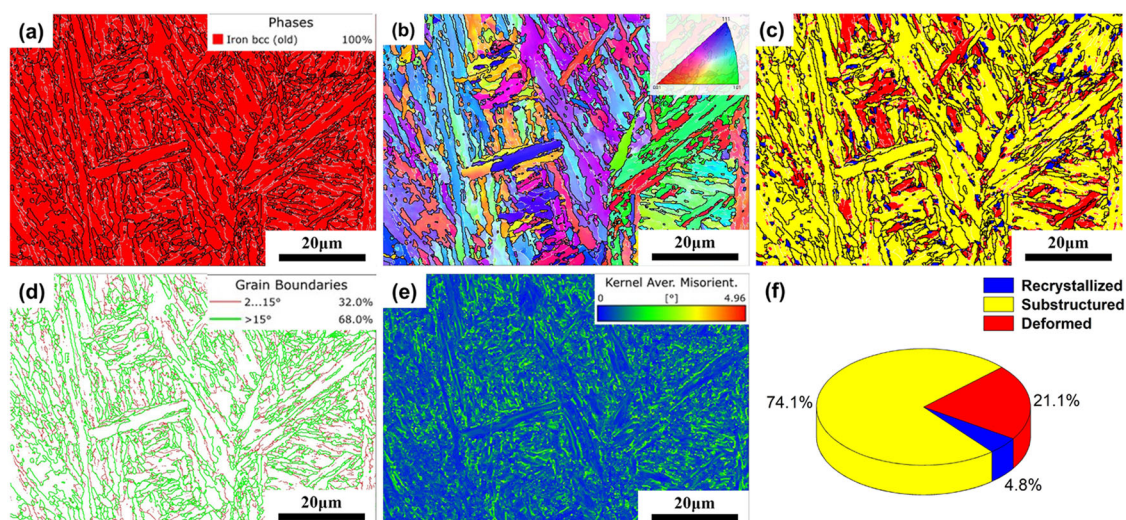

Fig. 2 | Microstructural analysis of R6 mooring chain steel. a Phase colored map; (**b**) Inverse Pole Figure (IPF) map; (**c**) recrystallization distribution diagram; (**d**) High-Angle Grain Boundary (GB) map; (**e**) Kernel Average Misorientation (KAM) map; (**f**) statistical result of the recrystallization distribution diagram.
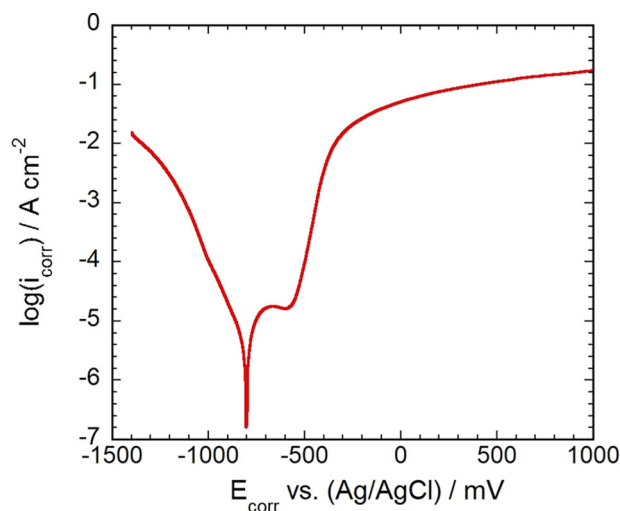
Fig. 3 | Potentiodynamic polarization curve of mooring chain steel at room temperature.
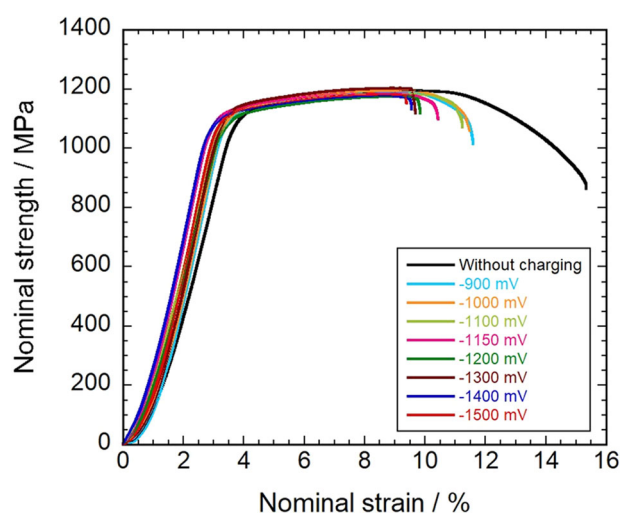

Fig. 4 | In-situ hydrogen charging tensile stress-strain curves of R6 mooring chain steel.

−1100 mV. This is also known as the hydrogen evolution transition potential of the material. The self-corrosion potential[27,28] of the specimen is determined to be −820 mV (Ag/AgCl) by extrapolation. Consequently, the hydrogen charging potential range of the in-situ tensile test was identified as −900 mV to −1500 mV (Ag/AgCl) for investigating the influence of cathodic protection potential on the hydrogen permeation behavior.

Mechanical properties

The strain-strength curves of the specimens at different polarization potentials were obtained, as shown in Fig. 4. Hydrogen charging has little effect on the tensile strength, while hydrogen charging significantly decreased the fracture elongation of the specimens at high negative polarization potentials.

The fracture elongation without charging specimen is 15.33%, while the elongation of the specimens at negative polarization potentials of 900, 1000, 1100, 1150, 1200, 1300, 1400, and 1500 mV is 11.59, 11.49, 11.24, 10.41, 9.83, 9.66, 9.53, and 9.36%, respectively. In contrast, with the potential of below −1150 mV, the hydrogen evolution reaction becomes more pronounced, and the early fracture of hydrogen-charged specimens occur[29,30]. Furthermore, it can be observed that there is a significant decrease in the post-fracture
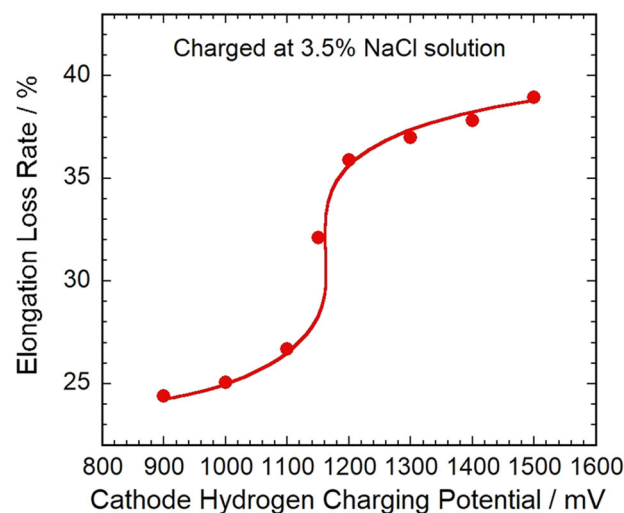

Fig. 5 | Relationship between the elongation loss rate and charging potential.

elongation rate between −1100 mV and −1200 mV, indicating a transition at this intermediate potential.

Figure 5 illustrates the relationship between HE susceptibility and hydrogen charging potential at different levels. Within the hydrogen charging potential range of −900 mV to −1100 mV, the increase in HE susceptibility is relatively low. However, when the hydrogen charging potential decreases the range of −1100 mV to −1200 mV, there is a transition in hydrogen embrittlement susceptibility. Furthermore, within the range of −1200 mV to −1500 mV, there is a gradual increase as the hydrogen charging potential becomes more negative. The findings indicate that there is a turning point in the HE susceptibility when the hydrogen charging potential is set at −1150 mV.

Thermal desorption analysis

Figure 6a shows the hydrogen desorption profiles of the hydrogen-charging specimens at different polarization potentials. All specimens exhibited hydrogen desorption peaks at approximately 400 K. It has been reported that the desorbed hydrogen corresponding to the peaks of 573 K is defined as diffusible hydrogen, which plays a critical role in HE[31,32].

An increase in diffusible hydrogen content is associated with a gradual decrease in elongation and an increase in plasticity loss rate in hydrogen-charged specimens (Fig. 6b, c). It is noteworthy that the HE susceptibility is low when the hydrogen concentration is less than 3 ppm. Additionally, there is a gradual increase in HE susceptibility as the hydrogen concentration exceeds 4.5 ppm. However, the hydrogen content reaches a turning point when the hydrogen charging potential is set at −1150 mV, which is consistent with the findings from Fig. 4 and Fig. 5.

Figure 7 shows the TDS profiles at different heating rates and active energy of hydrogen desorption. The activation energy for hydrogen desorption is 18.17 kJ mol^{-1}. Hydrogen traps in steel can generally be classified into irreversible traps and reversible traps. Traps with lower activation energy, such as lattice imperfections, grain boundaries, and dislocations, are considered reversible, whereas traps with higher activation energies, such as inclusions and precipitates, are considered irreversible[33]. Usually, the desorption activation energy smaller than 30 kJmol^{-1} is categorized as reversible hydrogen traps[34]. The hydrogen trapping sites in the tested steel are believed to be the grain boundary and lath boundary[35].

Characterization of the fracture surfaces

To further investigate the fracture behavior of the specimens, SEM observations were made on the fracture surfaces of both hydrogen-charged and non-hydrogen-charged specimens following tensile testing. For the non-hydrogen-charged specimen (Fig. 8a, b), a uniform distribution of equiaxed dimples were observed at both the center and the edges of the fracture surface,

Fig. 6 | Relationship between hydrogen content and elongation at break and the elongation loss rate. a TDS curves of specimens with different hydrogen charging potentials in 3.5% NaCl solution; (**b**) relationship between the elongation at break and hydrogen content; (**c**) relationship between the elongation loss rate and hydrogen content.
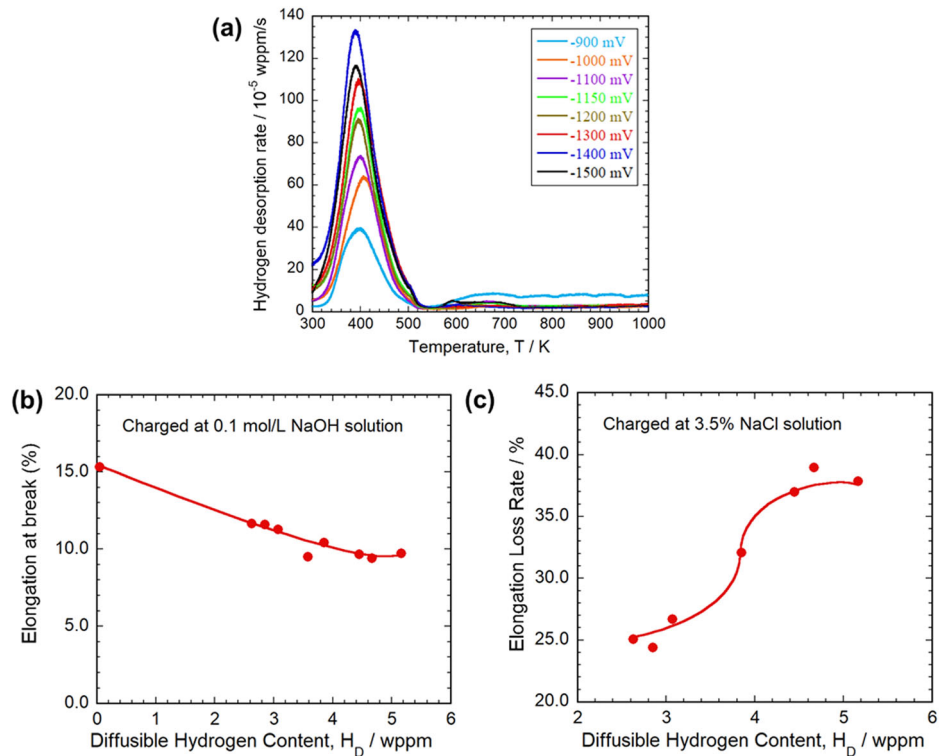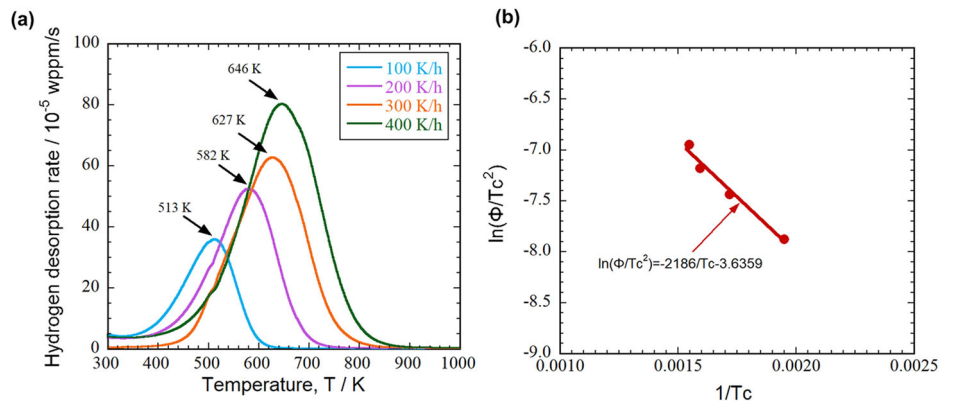

Fig. 7 | Activation energy of R6 mooring chain steel. a TDS curves of specimens with different heating rates; (**b**) activation energy of hydrogen desorption obtained by plots of ln (Φ/Tc^2) against 1/Tc.

which indicated the specimen have the typical ductile fracture behavior. When the cathodic hydrogen charging potential was set to −1000 mV (Fig. 8 c, d), the central region of the fracture surface continued to exhibit characteristics of ductile fracture, while a small amount of brittle fracture features appeared at the edges of the fracture surface. As the hydrogen charging potential became more negative, leading to an increase in hydrogen concentration within the specimens, the fracture mode progressively shifted towards brittle fracture. At a hydrogen charging potential of −1150 mV (Fig. 9a, b), the fracture of the specimens extended radially from the center with a mixed mode of intergranular and quasi-cleavage fracture[36,37], representing an intermediate transition state between ductile and brittle fracture modes. For a cathodic hydrogen charging potential of −1500 mV (Fig. 9c, d), the equiaxed dimples at the center of the specimen had completely disappeared, and the fracture mode had transitioned to a fully intergranular fracture.

Therefore, for high-strength steels exposed to overprotected CP systems, excessively negative protective potentials not only fail to provide protection but also induce intergranular cracking[38,39].

Relationship between the cracking zone size and charging potential

The hydrogen diffusion coefficient is a physical parameter that describes the diffusion behavior of hydrogen in materials. It quantifies the rate and efficiency of hydrogen atom propagation within the material[40]. Filho[41] conducted measurements of hydrogen concentration in samples placed at room temperature for varying durations and obtained a curve depicting the variation of hydrogen concentration with time. They derived a diffusion model for hydrogen in long cylindrical samples and derived the relationship formula (1):

$$C_t = C_\infty + 0.72(C_0 - C_\infty)\exp\left(-\frac{22.2D_e t}{d^2}\right) \qquad (1)$$

where, t represents the duration of sample placement, expressed in h. C_t represents the mass fraction of hydrogen in the steel, expressed in ppm. C_∞ represents the mass fraction of hydrogen in the experimental steel at time $t = \infty$, also expressed in ppm. C_0 represents the mass fraction of hydrogen in
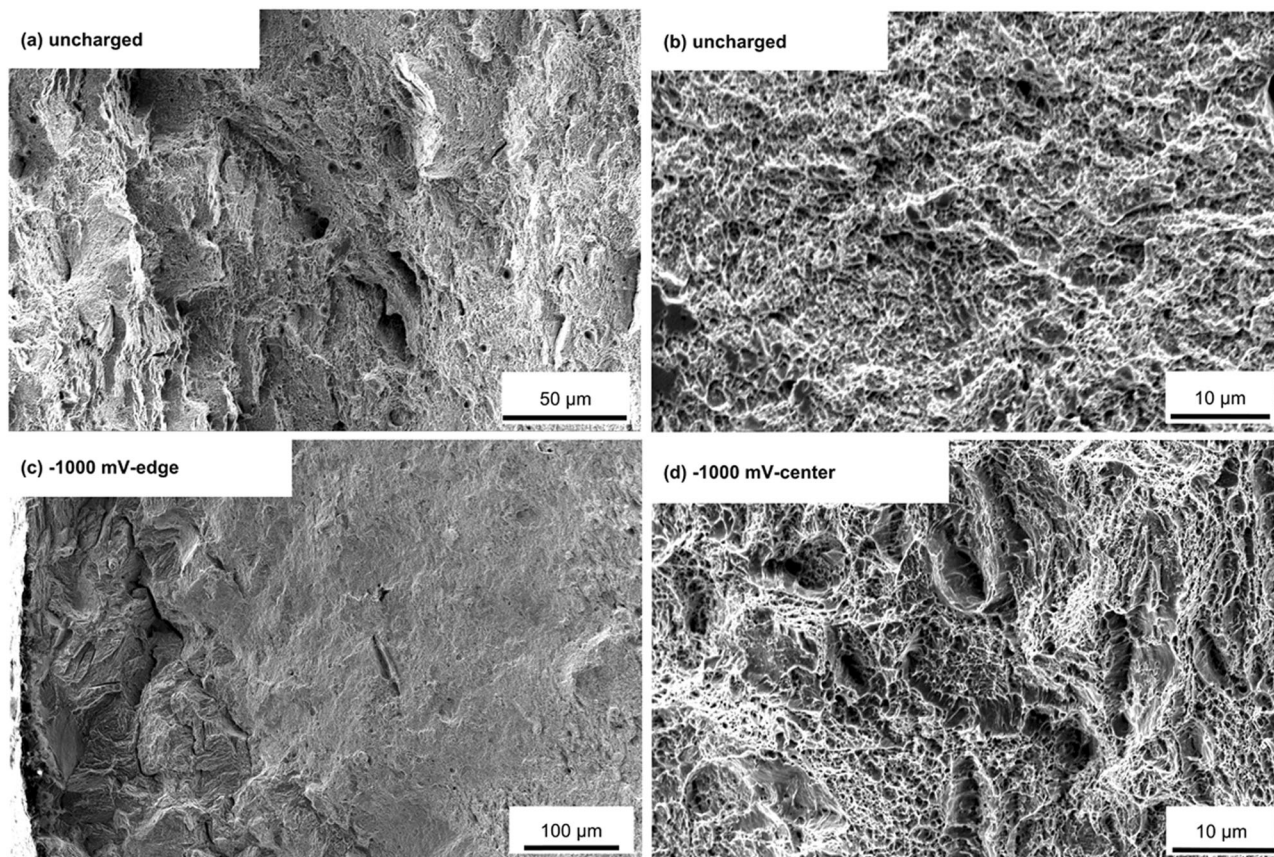
Fig. 8 | Fracture surfaces of R6 mooring chain steel after SSRT tests in 3.5% NaCl. a, b in air, (**c, d**) at −1000 mV; (**a, c**) represent the cracking initiation region for each specimen, while (**b, d**) correspond to the tensile fracture morphology at the fracture center.

the experimental steel at time $t = 0$, again expressed in ppm. d represents the diameter of the sample in cm. D_e represents the diffusion coefficient of hydrogen in the experimental steel, expressed in $cm^2 \, s^{-1}$. Given the sample d, the D_e can be determined.

As depicted in Fig. 10c, the hydrogen concentration in the sample exhibits an exponential decrease with increasing duration of ambient temperature exposure. By fitting the decay curve and utilizing the appropriate formula, the D_e in the tested steel was determined to be $6.4 \times 10^{-7} cm^2 \, s^{-1}$. It can be inferred that the diffusion rate of hydrogen is relatively low[42].

By observing the fracture surfaces of dynamically hydrogen-charged specimens (Fig. 10a, b). The observed initiation zone exhibits a fan-shaped pattern. Eight measurements were conducted to determine the distance from the vertex to the arc and subsequently averaged to obtain a representative value. It was found that the depth of the hydrogen-induced brittle fracture zone increases with a more negative hydrogen-charging potential (Fig. 10d). However, at a hydrogen-charging potential of −1200 mV, the increase in the depth of the brittle fracture zone becomes more gradual as the potential becomes more negative. This behavior can be attributed to the vacancy diffusion mechanism within the crystal lattice, which is the primary mode of hydrogen diffusion in metals. During hydrogen diffusion, hydrogen atoms need to jump through vacancies in the lattice[43]. As the diffusion distance of hydrogen in the metal increases, the number of available vacancies along the diffusion path decreases[44], thereby impeding further diffusion of hydrogen atoms.

Observations were made on the side surface of the hydrogen-charged tensile specimens using OM. As shown in Fig. 11, no cracks were observed on the surface of the hydrogen-uncharging specimen. However, when the polarization potential was set to −900 mV (Fig. 11b), hydrogen-induced cracks were clearly observed near the fracture surface of the specimen from

the side view. Furthermore, as the cathodic polarization potential became more negative, indicating an increased hydrogen content, it was observed that the number of hydrogen-induced cracks on the side surface of the specimen significantly increased, and the crack lengths were relatively short.

Micrograph of the side surface of the fractured tensile tested sample observed by EBSD

To study the microstructure near the fracture edge of the tensile specimen, Fig. 12a shows obvious necking of hydrogen-uncharged specimen, which was consistent with the fracture surface morphology. Figure 12c, d presents the IPF map of the region after the fracture of the tensile specimen. It can be observed from the figure that the color contrast of multiple grains has changed, indicating rotational grain motion and orientation[12] variation during the deformation process. During the tensile process, the grains in the sample are elongated along the tensile direction. This results in a continuous decrease in the proportion of HAGBs and a significant increase in LAGBs. This phenomenon is possibly attributed to the increased dislocation motion under the tensile load, subsequently inducing the formation of more substructures or LAGBs[39,45].

Figure 13 shows the recrystallization distribution and its statistical results of the tensile specimens whether it was charged with hydrogen or not. As can be seen from Fig. 13a, c, there is almost no recrystallization in the hydrogen un-charging tensile specimen, with only 2.82% of the recrystallized grains, 69.31% deformed and 27.87% reverted grains, respectively. As can be seen from Fig. 13b, d, the deformed, recovered and recrystallized grains of −1400 mV hydrogen-charging tensile specimen were 79.68%, 17.02%, and 3.3%, respectively.
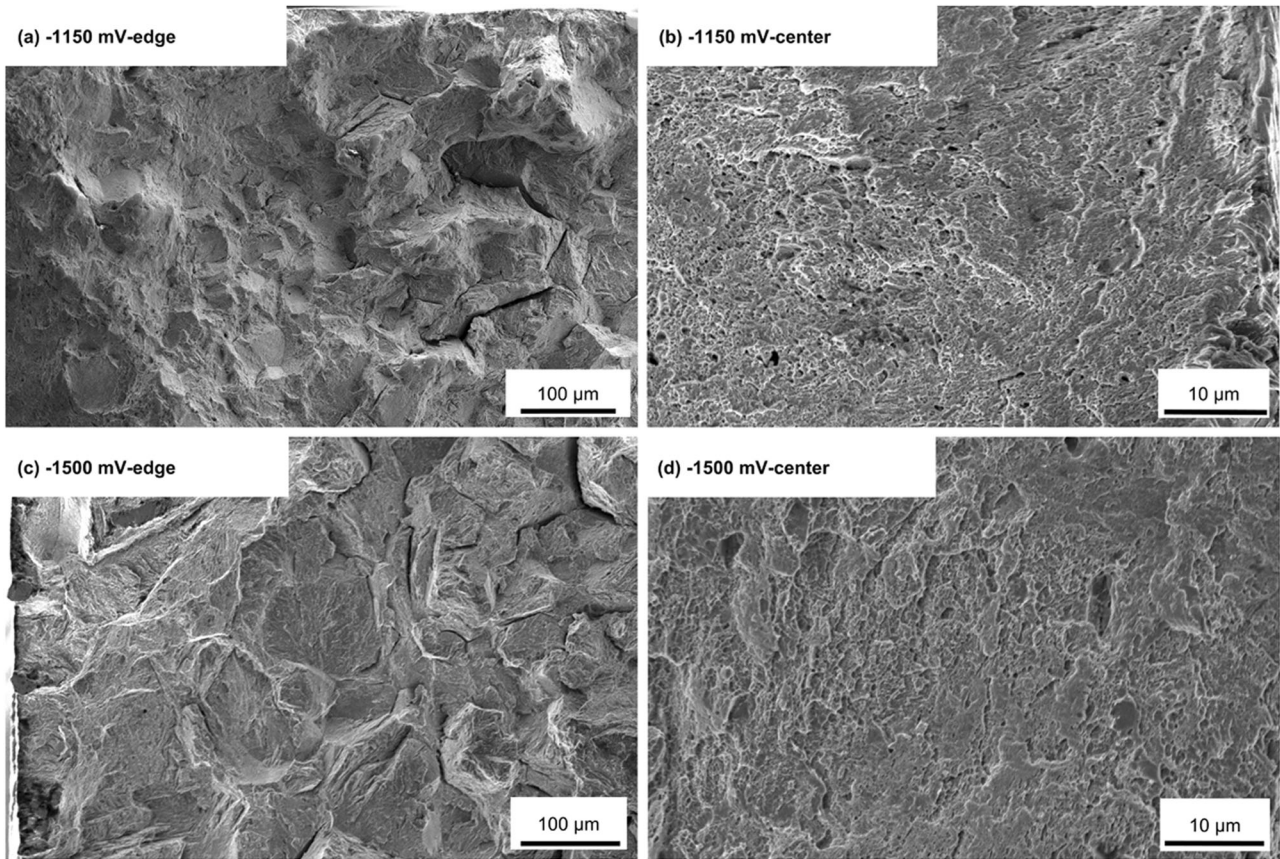
Fig. 9 | Fracture surfaces of R6 mooring chain steel after SSRT tests in 3.5% NaCl. a, **b** at −1150 mV, (**c, d**) at −1500 mV; (**a, c**) represent the cracking initiation region for each specimen, while (**b, d**) correspond to the tensile fracture morphology at the fracture center.

Fig. 10 | Cross-section fracture surface of specimens. a −1150 mV and (**b**) −1500 mV; (**c**) diffusion coefficient of hydrogen in the tested steel; (**d**) the relationship between the crack initiation region size and the hydrogen charging potential.
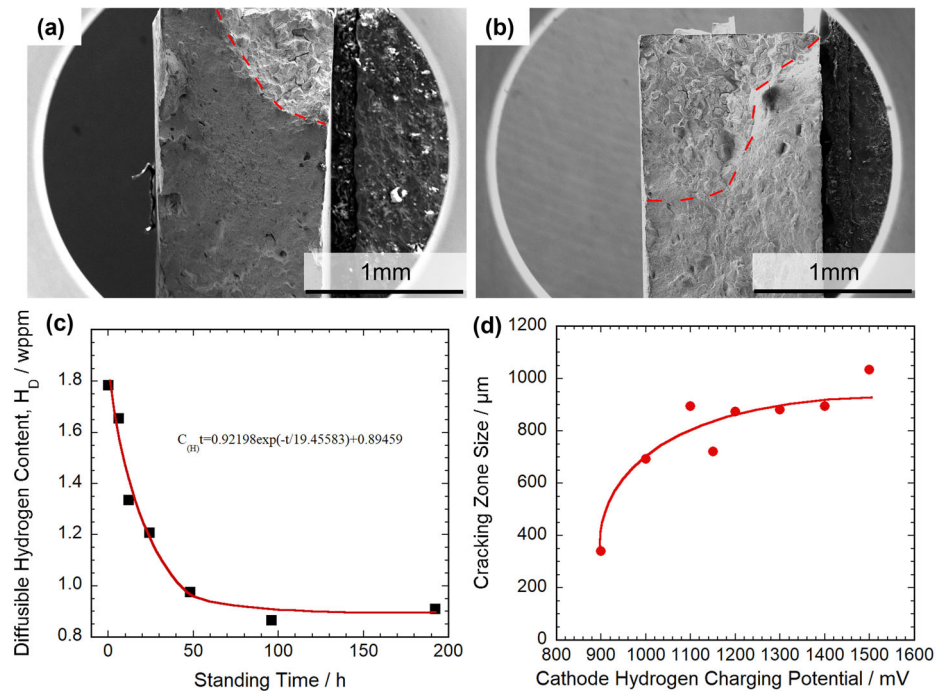

$$C_{(H)}t = 0.92198\exp(-t/19.45583) + 0.89459$$

Fig. 11 | OM images of the fractured specimen side after tensile testing. a without hydrogen charging specimen, (**b**) −900 mV, (**c**) −1150 mV, (**d**) −1400 mV.
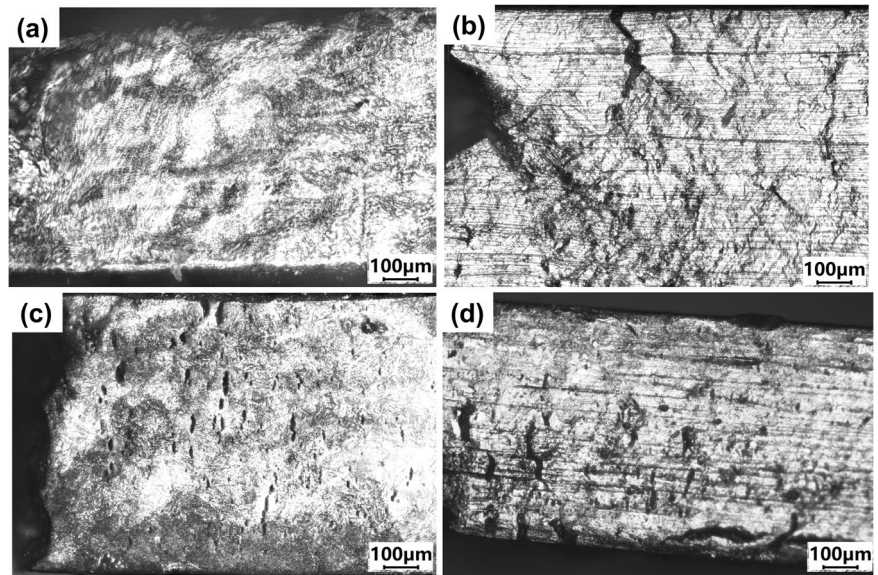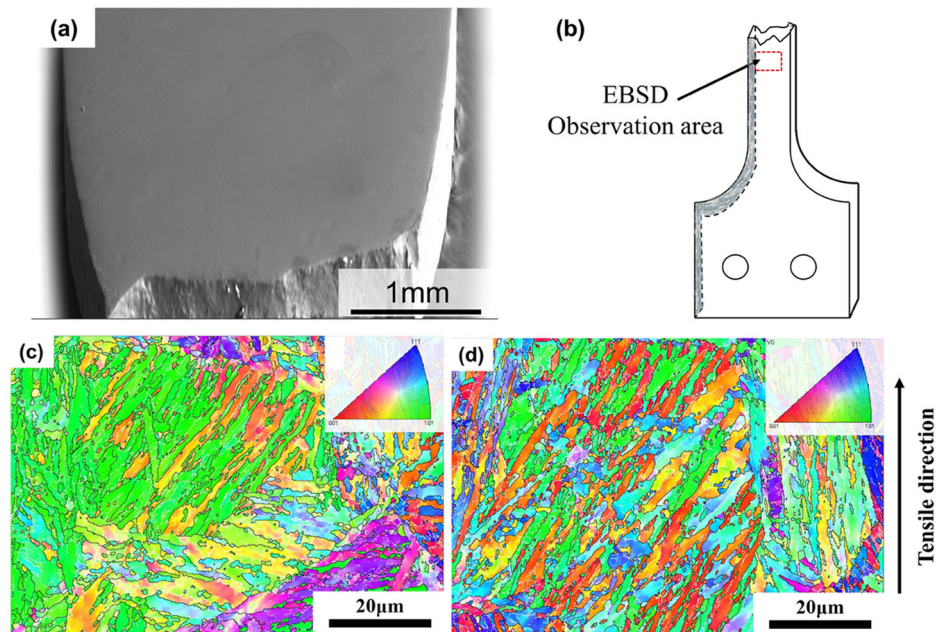

Fig. 12 | Observation specimens after tensile test. a representative tensile cross-section SEM image of the fractured specimen; (**b**) schematic image of the specimen after tensile test and EBSD observation area; (**c**) IPF map of the hydrogen-uncharging specimen; (**d**) IPF map of the hydrogen-charging specimen.

After the tensile tests, deformed twins were observed in both samples, shown in the red line in Fig. 13a, c. The proportion of hydrogen un-charging and hydrogen-charging specimens was 6.8% and 5.51%, respectively. It is evident from the deformed EBSD observations that the uncharged specimen showed a higher twin density compared to the hydrogen-charging specimen, suggesting that the hydrogen-charging sample has higher plasticity[46]. The specimen interactions occur with microstructural defects, such as dislocations upon hydrogen charging. These interactions may lead to a reduction in the activation energy required for dislocation movement, thereby facilitating dislocation motion and multiplication, which results in localized plastic deformation. Hydrogen atoms have an increased amount of time to interact with dislocations under conditions of slow strain rate, resulting in enhanced plastic deformation and the mount of deformed grains was increased.

KAM can be utilized to understand the local distortions, grain orientation change, and dislocation density level of metals[47]. Figure 14b, e represent the distribution map of KAM in the sample under different conditions. The KAM values are depicted by colors, with red and blue representing the highest and lowest values, respectively. Regions with higher numerical values indicate dislocation density[34,48], suggesting significant crystal deformation and distortion during the tensile process.

During the process of in-situ tensile, the KAM values are shown in Table 1. Figure 14c, f shown the KAM diagram of the tensile specimens. Due to the large plastic deformation, the KAM value of 0.9 for the hydrogen un-charging specimen (15.33% strain) is greater than the original sample (Fig. 2e). Under the hydrogen charging condition of −1400 mV, the KAM value is 0.96, which differs only slightly from the KAM value of the tensile specimen without hydrogen charging. The hydrogen concentration is relatively high at 5.17 wppm under the

Fig. 13 | Recrystallization distribution diagrams and statistical results. a, **c** uncharged specimen, (**b**, **d**) hydrogen charging specimen.
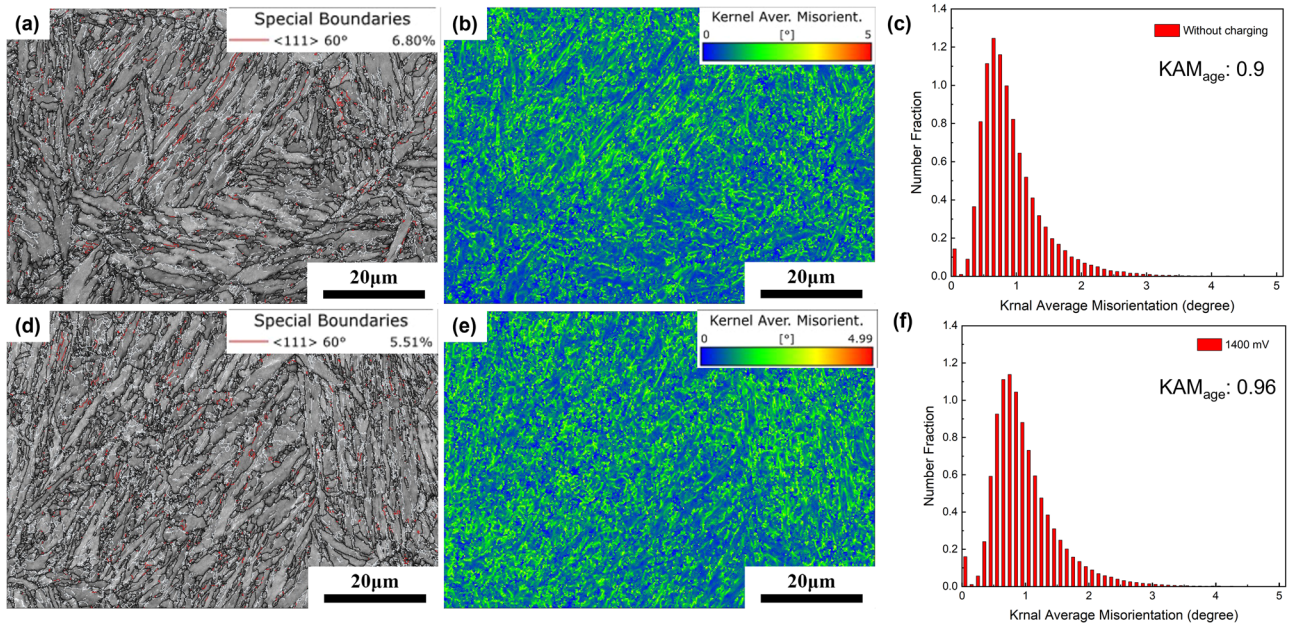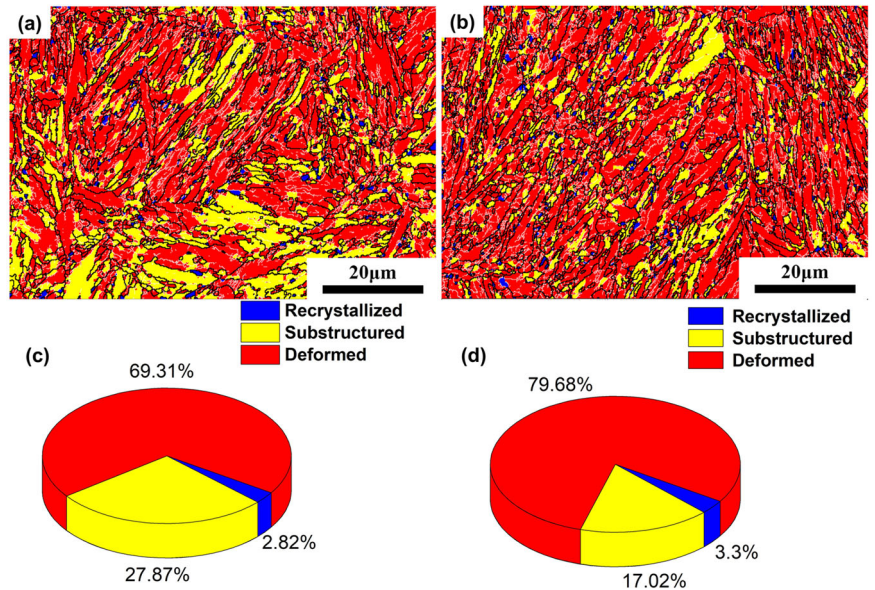

Fig. 14 | EBSD images of microstructure of the tensile specimen. a, b, c uncharged sepcimen and (**d, e, f**) hydrogen charging specimen. **a, d** IQ maps, **b, c, e, f** KAM maps and the statistical results.

Table 1 | The results of KAM of R6 before and after the hydrogen charging plastic deformation

Sample	Original sample	Without charging	Charging at −1400 mV
KAM value	0.66	0.9	0.96

Table 2 | Chemical composition of mooring chain steel (wt.%)

C	Ni	V	Mn	Si	P	S	Fe
0.29	4.5	0.03	0.35	0.21	0.006	0.002	Bal.

condition of −1400 mV, which lead to the presence of hydrogen atoms during the tensile process. This presence promotes internal stress concentration within the crystals[45,49], resulting in premature fracture of the specimen. Consequently, the KAM value differs from that of the tensile specimen without hydrogen charging by only 0.06.

Methods
Material
The ultra-high-strength mooring chain steel for fixed offshore platforms was investigated in this study, which was provided by Jiangsu Asian Star Anchor Chain Co., Ltd. The chemical composition of the steel is listed in Table 2.

Electrochemical test

The electrochemical measurements were carried out in a three-electrode cell. The electrochemical workstation (PARSTAT MC) was employed to measure the potentiodynamic polarization curves. A platinum foil and an Ag/AgCl electrode (in a 0.1 mol L^{-1} KCl solution) were used as the counter and reference electrodes, respectively. The specimen was used as the working electrode. Before the experiments, the working electrode was allowed to undergo free corrosion until it reached a stable open circuit potential. The measurements were conducted with a scan rate of 0.33 mV s^{-1} within the range of -1500 mV to 1000 mV. All electrochemical experiments were performed at least three times to ensure reproducibility.

In situ conventional potentiostatic hydrogen charging

In-situ slow strain rate (SSRT) tests were conducted in a 3.5% NaCl aqueous solution. The sizes of the tensile specimens as shown in Fig. 15.

Before the SSRT, the specimen was pre-charged with hydrogen in 3.5% NaCl solution for a duration of two hours. The reference electrode and the counter electrode were Ag/AgCl electrode and Pt sheet, respectively. Subsequently, an in-situ hydrogen charging tensile test was immediately conducted at the same potential, as shown in Fig. 16. The crosshead speed was set at 0.005 mm min^{-1}, corresponding to a nominal strain rate of 5.21×10^{-6} s^{-1}. The fractured specimens were promptly cleaned with acetone and immediately immersed in liquid nitrogen until they were ready for TDS measurements.
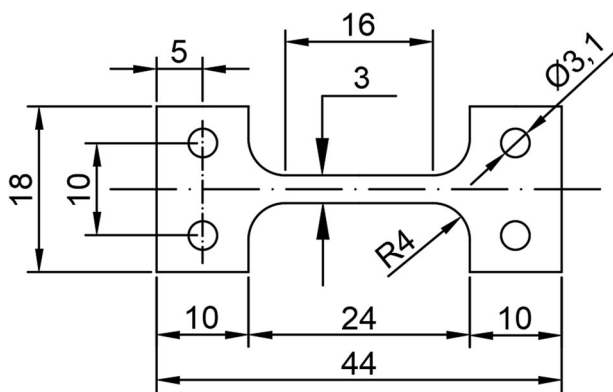

Fig. 15 | Dimensions of the in-situ tensile specimen (mm).

The relative elongation loss (δ_L) was defined as the hydrogen embrittlement (HE) susceptibility using the following equation[50]:

$$\delta_L = \frac{(\delta_0 - \delta_H)}{\delta_0} \times 100\% \qquad (2)$$

where δ_0 and δ_H represent the elongation of the hydrogen-uncharging and hydrogen-charging specimens, respectively.

Thermal Desorption Analysis

The hydrogen concentrations in the hydrogen-precharged specimens were measured with thermal desorption spectroscopy (HTDS-003, R-DEC Co., Ltd), which has a 0.01 wppm (wt%) accuracy. The TDS measurements were performed from room temperature (RT) to 1073 K with heating rates of 100–400 K h^{-1}, and the corresponding hydrogen desorption rates were recorded.

After sectioning the fracture for SEM, a segment measuring 5 mm is excised for subsequent hydrogen concentration testing. In addition, cylindrical specimens with a diameter of 10 mm and a length of 20 mm were hydrogen-charged at a current density of 1 mA cm^{-2}, and then TDS was conducted at heating rates of 100, 200, 300, and 400 K h^{-1}. The activation energy (E_a) for hydrogen de-trapping was calculated on the following Kissinger equation[51]:

$$\frac{\partial(In \frac{\Phi}{T_c^2})}{\partial(\frac{1}{T_c})} = -\frac{E_a}{R} \qquad (3)$$

where Φ, T_c, and R are the heating rate, peak temperature at which the maximum of hydrogen-charged specimens desorption rate occurs, and gas constant, respectively.

Microstructures and fracture surface analysis

The microstructure of the specimen was observed by scanning electron microscope (SEM: JSM 7500 F), equipped with an electron back-scattered diffraction (EBSD: Thermo Scientific/Helios G4 CX system). The EBSD measurements were performed with an acceleration voltage of 20 kV and a step size of 0.2 μm. In addition, the fracture surfaces of hydrogen-uncharging and hydrogen-charging specimens were observed by SEM.

Fig. 16 | Schematic diagram of in situ hydrogen charging and tensile testing.
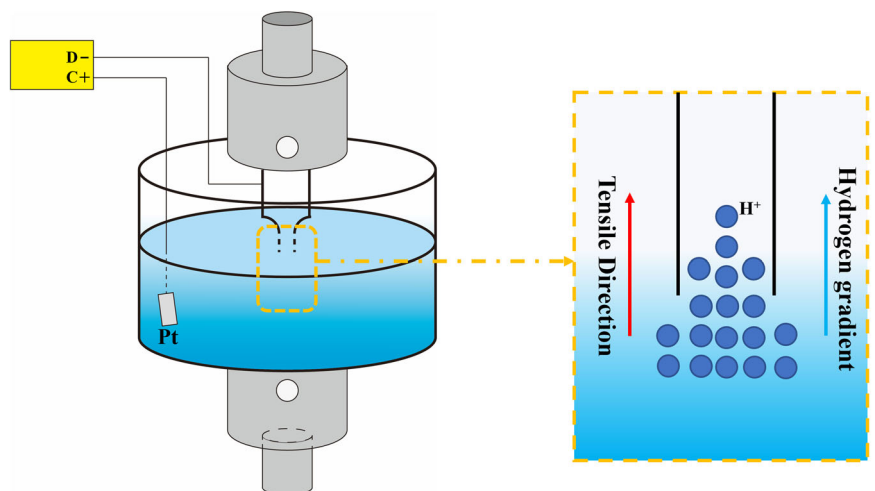
Data availability

All data needed to evaluate the conclusions in the paper are presented in the paper. Additional data related to this paper are available from the corresponding author upon reasonable request.

References

1. Xue, X., Chen, N. & Pu, Y. Mooring fatigue assessment evaluating chain twist and out-of-plane bending for a semi-submersible. *J. Offshore Mech. Arct. Eng.* **142**, 1–22 (2020).
2. Rogers, H. Hydrogen embrittlement of metals: atomic hydrogen from a variety of sources reduces the ductility of many metals. *Sci.* **159**, 1057–1064 (1968).
3. Hirth, J. Effects of hydrogen on the properties of iron and steel. *Met. Mater. Trans. A* **11**, 861–890 (1980).
4. Nagumo, M. Function of hydrogen in embrittlement of high-strength steels. *ISIJ Int* **41**, 590–598 (2001).
5. ABS, Requirements for the Certification of Offshore Mooring Chains. (2022).
6. Lillestøl, D.-B. & Pedro, B. High-Strength Mooring Chains-Rules and Standards Updates for Improved Usability and Suitability. *ISOPE*. (2023).
7. Barros, P. et al. Review of Available Material on Usability and Suitability of High Strength Mooring Chain. *ISOPE*. (2023).
8. Nevshupa, R., Martinez, I. & Ramos, S. The effect of environmental variables on early corrosion of high strength low-alloy mooring steel immersed in seawater. *Mar. Struct.* **60**, 226–240 (2018).
9. Lopez-Ortega, A. et al. Influence of temperature on the corrosion and tribocorrosion behaviour of High-Strength Low-Alloy steels used in offshore applications. *Tribol. Int.* **121**, 341–352 (2018).
10. Zhang, X. et al. Corrosion form transition of mooring chain in simulated deep-sea environments: remarkable roles of dissolved oxygen and hydrostatic pressure. *J. Mater. Sci. Technol.* **162**, 118–130 (2023).
11. Zhang, X. et al. The pitting to uniform corrosion evolution process promoted by large inclusions in mooring chain steels. *Mater. Charac*. **181** (2021).
12. Zhang, X., Wu, W., Fu, H. & Li, J. The effect of corrosion evolution on the stress corrosion cracking behavior of mooring chain steel. *Corros. Sci.* **203** (2022).
13. Mendoza, J., Haagensen, P. J. & Khler, J. Analysis of fatigue test data of retrieved mooring chain links subject to pitting corrosion. *Mar. Struct*. **81** (2022).
14. Qvale, P., Nordhagen, H. O., As, S. K. & Skallerud, B. H. Effect of long periods of corrosion on the fatigue lifetime of offshore mooring chain steel. *Mar. Struct*. **85** (2022).
15. Li, S. Study of the hydrogen delayed fracture of mooring chain steel using strain rate testing. *Int. J. Electrochem.* **14**, 9221–9230 (2019).
16. Li, S. Hydrogen embrittlement behavior of ultrahigh strength mooring chain steel evaluated by the slow strain rate test. *Int. J. Electrochem.* **14**, 2705–2713 (2019).
17. Albisu, B. et al. New Grades of High Strength Steel for Offshore Mooring Chains: R5S (1100MPa) and R6 (1200 MPa). *OTC*. D041S055R003 (2016).
18. Garikoitz, A., Alberto, A., Fernández-Calvo, A. & Javier, A. Hydrogen embrittlement susceptibility of r4 and r5 high-strength mooring steels in cold and warm seawater. *Metals* **8**, 700 (2018).
19. Osvoll, H., Wigen, S. W. & Green, L. M. Mooring Chains - Extent of Drain from Iccp System and Sacrificial Cp System. *NACE*. NACE-09066 (2009).
20. ABS, Guidance Notes on Cathodic Protection of Offshore Structures. (2018).
21. DNV-RP-B401, Cathodic protection design. (2021).
22. Yin, S. H. et al. Investigating the thermal stability of compressive residual stress in a gradient nanostructured austenitic stainless steel by in-situ XRD and TEM. *Mater. Charact.* **207**, 11361 (2024).
23. Joshua, O. et al. In situ SR-XRD analysis of corrosion product formation during 'pseudo-passivation' of carbon steel in CO_2-containing aqueous environment. *Corros. Sci.* **225**, 111598 (2023).
24. Gussev, M. N. & Leonard, K. J. In situ sem-ebsd analysis of plastic deformation mechanisms in neutron-irradiated austenitic steel. *J. Nuc. r. Mater.* **517**, 45–56 (2019).
25. Rizwan, M. et al. Microstructural and texture evolution investigation of laser melting deposited ta15 alloy at 500 °C using in-situ ebsd tensile test. *Mat Sci Eng A-Struct*. **857** (2022).
26. Liu, Z. et al. Unraveling the effect of long-term aging on hydrogen-aided cracking behavior in a maraging stainless steel. *J. Mater. Eng. Perform.* **32**, 4306–4314 (2023).
27. Wang, Z., Feng, Z., Fan, X. H. & Zhang, L. Pseudo-passivation mechanism of cocrfenimo_(0.01) high-entropy alloy in H_2S-containing acid solutions. *Corros. Sci.***179** (2021).
28. Kim, Y. S., Lee, S. K., Chung, H. J. & Kim, J. G. Influence of a simulated deep sea condition on the cathodic protection and electric field of an underwater vehicle. *Ocean Eng.* **148**, 223–233 (2018).
29. Koyama, M. Quantification and characterization of microdamage resistance in metals for designing high-strength ductile microstructures. *Acc. later. Res.* **2**, 1167–1176 (2021).
30. Koyama, M. et al. Effect of hydrogen content on the embrittlement in a Fe-Mn-C twinning-induced plasticity steel. *Corros. Sci.* **59**, 277–281 (2012).
31. Belyaev, A. K. Multichannel diffusion vs tds model on example of energy spectra of bound hydrogen in 34crnimo6 steel after a typical heat treatment. *Int. J. Hydrogen Energ.* **41**, 8627–8634 (2016).
32. Raina, A., Deshpande, V. S. & Fleck, N. A. Analysis of thermal desorption of hydrogen in metallic alloys. *Acta later* **144**, 777–785 (2018).
33. Zhang, S. et al. Dual role of nanosized NbC precipitates in hydrogen embrittlement susceptibility of lath martensitic steel. *Corros. Sci.* **164** (2020).
34. Gui, L. et al. Study on the improving effect of Nb-V microalloying on the hydrogen induced delayed fracture property of 22MnB5 press hardened steel. *Mater. Des.* **227**, 111763 (2023).
35. Li, X. et al. Effect of tempering temperature and inclusions on hydrogen-assisted fracture behaviors of a low alloy steel. *Mater. Sci. Eng. A.* **682**, 359–369 (2017).
36. Hong, Y. et al. Strain-induced twins and martensite: Effects on hydrogen embrittlement of selective laser melted (SLM) 316 L stainless steel. *Corros. Sci*. **208** (2022).
37. Park, I. J. et al. The effect of Ti precipitates on hydrogen embrittlement of Fe-18Mn-0.6C-2Al-xTi twinning-induced plasticity steel. *Corros. Sci.* **89**, 38–45 (2014).
38. Cheng, X. et al. The Character of Hydrogen Embrittlement in Mooring Chain Steel. *JOM* **72**, 2003–2010 (2020).
39. Mohtadi-Bonab, M. A. et al. An extensive study of hydrogen-induced cracking susceptibility in an API X60 sour service pipeline steel. *Int. J. Hydrog. Energy* **41**, 4185–4197 (2016).
40. Claeys, L. et al. Critical assessment of the evaluation of thermal desorption spectroscopy data for duplex stainless steels: A combined experimental and numerical approach. *Acta Mater.* **186**, 190–198 (2020).
41. Carneiro, C. J. et al. The effect of hydrogen release at room temperature on the ductility of steel wire rods for pre-stressed concrete. *Mater. Sci. Eng. A.* **527**, 4947–4952 (2010).
42. Duportal, X. S. On the estimation of the diffusion coefficient and distribution of hydrogen in stainless steel. *Scr. Mater.* **186**, 282–286 (2020).
43. Kholtobina, A. S. et al. Hydrogen trapping in bcc iron. *Mater* **13**, 2288 (2020).
44. Sato, R. & Takai, K. Quantitative hydrogen trap states on high-angle grain boundaries and at dislocations in iron. *Scr. mater.* **228**, 115339 (2023).

45. Mohtadi-Bonab, M. A., Masoumi, M. & Szpunar, J. A. A comparative fracture analysis on as-received and electrochemically hydrogen charged API X60 and API X60SS pipeline steels subjected to tensile testing. *Eng. Failure Anal*. **129** (2021).

46. Liu, J. et al. Significance of melt pool structure on the hydrogen embrittlement behavior of a selective laser-melted 316L austenitic stainless steel. *Mater.* **16**, 1741 (2023).

47. Wang, X., Zhang, Y., Li, H. & Huang, M. Y. In-situ ebsd study of the degradation behavior in a type 316 austenitic stainless steel during plastic deformation. *J. Strain Anal. Eng. Des.* **56**, 587–597 (2021).

48. Mohtadi-Bonab, M. A. et al. Effect of different microstructural parameters on hydrogen induced cracking in an API X70 pipeline steel. *Met. Mater. Int.* **23**, 726–735 (2017).

49. Nolze, G., Maria, J., Jürgen, O. & Winkelmann, A. Improving the precision of orientation measurements from technical materials via ebsd pattern matching. *Acta Mater.* **159**, 408–415 (2018).

50. Fan, Y. H., Zhang, B., Wang, J. Q., Han, E. H. & Ke, W. Effect of grain refinement on the hydrogen embrittlement of 304 austenitic stainless steel. *J. Mater. Sci. Technol.* **35**, 2213–2219 (2019).

51. Kang, H. J. et al. Effect of nano-carbide formation on hydrogen-delayed fracture for quenching and tempering steels during high-frequency induction heat treatment. *Mat. Sci. Eng. A-Struct.* **543**, 6–11 (2012).

Author contributions

J.J.W.: Conceptualization, methodology, original manuscript writing, experimental work, and data interpretation. K.H., F.Y., Z.P.C., J.L., and M.L.: Experimental work, data interpretation. Y.L.S., M.J.L., X.M.Y., J.Y.Z., Y.T.Z., Y.P.Y., D.H.P., and Y.L.: Manuscript review and editing. S.J.L.: Program management, manuscript review, and editing.

Competing interests

The authors declare no competing interests.

Additional information

Correspondence and requests for materials should be addressed to Songjie Li.

Reprints and permissions information is available at http://www.nature.com/reprints

Publisher's note Springer Nature remains neutral with regard to jurisdictional claims in published maps and institutional affiliations.